

# Soft Activation Mapping of Lung Nodules in Low-dose CT Images

Yiming Lei<sup>1</sup>, Yukun Tian<sup>1</sup>, Hongming Shan<sup>2</sup>, Junping Zhang<sup>1</sup>, Ge Wang<sup>2</sup>, Mannudeep Kalra<sup>3</sup>

<sup>1</sup>Department of Computer Science, Fudan University, Shanghai 200082, China

<sup>2</sup>Department of Biomedical Engineering, Rensselaer Polytechnic Institute, Troy, NY 12180 USA

<sup>3</sup>Department of Radiology, Massachusetts General Hospital, Harvard University, Boston, MA 02114 USA  
{17110240016, 17210240203, jpzhang}@fudan.edu.cn, {shanh, wangg6}@rpi.edu, mkalra@mgh.harvard.edu

## Abstract

As a popular deep learning model, the convolutional neural network (CNN) has produced promising results in analyzing lung nodules and tumors in low-dose CT images. However, this approach still suffers from the lack of labeled data, which is a major challenge for further improvement in the screening and diagnostic performance of CNN. Accurate localization and characterization of nodules provides crucial pathological clues, especially relevant size, attenuation, shape, margins, and growth or stability of lesions, with which the sensitivity and specificity of detection and classification can be increased. To address this challenge, in this paper we develop a soft activation mapping (SAM) to enable fine-grained lesion analysis with a CNN so that it can access rich radiomics features. By combining high-level convolutional features with SAM, we further propose a high-level feature enhancement scheme to localize lesions precisely from multiple CT slices, which helps alleviate overfitting without any additional data augmentation. Experiments on the LIDC-IDRI benchmark dataset indicate that our proposed approach achieves a state-of-the-art predictive performance, reducing the false positive rate. Moreover, the SAM method focuses on irregular margins which are often linked to malignancy.

## Introduction

Lung cancer is one of the most fatal malignant diseases. According to the World Health Organization, there will be ten million deaths from lung cancer by the year 2030 (WHO 2011). To reduce the mortality of lung cancer, several challenges must be addressed including the histologic and genetic heterogeneity of lung cancers and other ailments that often co-exist with lung cancer due to shared risk factor of smoking such as coronary heart disease and chronic obstructive lung diseases (Team 2011). Early detection of lung cancer with low dose CT (LDCT) has been recently approved in some countries including the United States to improve patient survival. However, LDCT has high false positive rate since many detected pulmonary nodules are benign. Radiologists rely on features such as lesion size, attenuation, and margins to assess likelihood of malignancy, and that triggers either follow up LDCT (for less suspicious

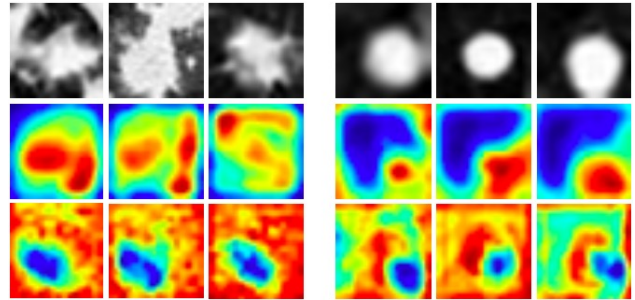


Figure 1: Lesion visualization. The first row illustrates different types of nodules, the second row shows the CAM (Zhou et al. 2016), and the third row is our SAM maps. The three left columns represent malignant nodules, and the three right columns display benign nodules.

nodules) or additional diagnostic testing (for more suspicious nodules). Most conventional and machine learning algorithms merely detect and measure solid pulmonary nodules above a certain size threshold. For this purpose, there are two steps in the traditional medical imaging domain: feature extraction such as using Local Binary Pattern (LBP) (Ahonen, Hadid, and Pietikainen 2007), and then nodule classification such as via SVM (Lei et al. 2017). Unlike deep learning, a major disadvantage of this scheme is its limited ability in representing various lung nodules.

Over the past decade, deep learning has made a tremendous progress in image classification. During the learning and decision processes, CNNs often exhibit shape bias, which is related to human cognitive psychology (Ritter et al. 2017), i.e., shape plays a dominant role in recognition behavior over color and texture. Motivated by this observation, our approach will refine the discriminative performance in categorizing pulmonary nodules on the basis of diverse variations of nodule bodies and margins.

Acting as a structural regularizer, Global average pooling (GAP) (Lin, Chen, and Yan 2014) was proposed to avoid the use of fully-connected (FC) layers. (Zhou et al. 2016) extended GAP to localize an object with a class activation mapping (CAM), in which the weights of the output layer are projected onto the final convolutional feature maps, maintaining considerable classification results. The CAM

approach is good at presenting specific objects in larger regions. Indeed, performing GAP directly on the final feature maps ignores the fine-grained local features. A disadvantage in doing so is that it is inaccurate for malignant lesion localization. Furthermore, (Shin et al. 2016; Li et al. 2004) pointed out that 1) if only performing a coarse localization in malignant and benign nodule regions, the performance of the predictive system will be degenerated; 2) to improve the lung nodule classification, it is necessary to perform a fine-grained localization so that discriminative lesion descriptors such as ground glass (GG), cavity (CA), micronodules (MN) and consolidation (CD) can be obtained. In order to address these issues, here we propose the soft activation mapping (SAM) to project final feature maps into single weights, allowing the preserved local features to have an impact on the final weights. Our experimental results show that SAM indeed focuses on relatively discrete and irregular margins which indicate a higher likelihood of malignancy for the corresponding nodule. Then, a high-level enhanced SAM (HESAM) re-utilizes features at higher convolutional layers to guarantee high accuracy and precise localization.

Another issue in machine learning based lung LDCT image analysis is the lack of labeled data because of the involved high annotation cost. A number of studies (Shan et al. 2017; Shen et al. 2015; Setio et al. 2016; Hussein et al. 2017) were conducted to automate this task to various degrees. However, none of the methods is totally satisfactory in extracting features from a whole CT image volume, which contains diverse features specific to categorization of nodules and individual characteristics. In this paper, we propose to take volume images of lung nodules into a 2D network for streamlined processing. Our experiments show that our method can achieve a state-of-the-art classification accuracy.

Our contributions in this paper are summarized as follows:

- SAM is introduced to localize lesions in fine-grained regions, facilitating lung nodule classification;
- HESAM is proposed to combine SAMs and high-level features to achieve the best performance of classification and localization;
- Multiple CT slices help alleviate overfitting, thereby improving the predictive performance in nodule classification.

## Related Work

Usually, lung screening and diagnosis with LDCT involve two steps: nodule localization and classification. In this section, we will give a brief survey on these two aspects.

**CNNs based classification.** One difficulty in lung nodule classification is a limited number of annotated CT slices. As in most deep learning studies, (Shan et al. 2017) augmented the set of lung nodule slices through rotation, flip and shift, etc. However, these simple operations are not effective enough for alleviating overfitting. (Setio et al. 2016) extracted 2D patches from nine symmetrical planes of a cube where a potential candidate locates at the center

of the corresponding patch. TumorNet (Hussein et al. 2017) obtained three candidates of one patch by projecting median intensity along three coordinate axes. Nevertheless, the features learned by these methods cannot cover the lesions over all slices.

**UNet based segmentation.** (Ronneberger, Fischer, and Brox 2015) proposed to conduct the medical image segmentation with the skip connection, which can convey the early features and combine them with features of later layers (Shan et al. 2018) so that high-resolution features can be preserved. (Dou et al. 2017) extracted volume candidates with various nodule diameters. These 3D CNNs learn more spatial information from different slices. An advantage is that the 3D network can retrace the success of the 2D network if a large amount of labeled data are available (Hara, Kataoka, and Satoh 2018). Furthermore, 3D-UNet (Çiçek et al. 2016; Wu et al. 2018) was proposed to segment volumetric medical data and conduct multi-task learning, by performing classification after the output layer of 3D-UNet.

**Class activation mapping via global average pooling.** Instead of adding FC layers on top of the features maps, (Lin, Chen, and Yan 2014) proposed GAP as a network in network (NIN) and fed the resultant vectors directly into the softmax layer. (Zhou et al. 2016) conducted GAP on the final feature maps, followed by one FC layer, with the resultant vector being fed into the softmax layer. The computation of the class activation map can be written as follows:

$$S_c = \sum_k \omega_k^c \sum_{x,y} f_k(x,y) = \sum_{x,y} \sum_k \omega_k^c f_k(x,y), \quad (1)$$

$$M_c(x,y) = \sum_k \omega_k^c f_k(x,y), \quad (2)$$

where  $F_k = \sum_{x,y} f_k(x,y)$  and  $f_k(x,y)$  are results of performing GAP on unit  $k$  and the activation of the last convolutional layer at unit  $k$  respectively.  $S_c$  is used as the input to the softmax.  $\omega_k^c$  represents the importance of  $F_k$  for class  $c$  (Zhou et al. 2016). This method can identify the extent of an object, and make sense for natural object localization. However, the shape and margin variation of malignant nodules may require more discriminative features. To address this issue, in the following we propose a new component consisting of average pooling and the FC layer following each final feature map.

## Methods

In this section, we describe our network in Fig.2 and soft activation mapping part in Fig.3.

### Proposed Model for Nodule Classification.

Our network begins with the input of multiple slices, and details of data preprocessing will be described in the Data Preparation section. Based on the structure of UNet, we apply its three down-sampling blocks and three up-sampling blocks to acquire a representative code of the input. This code is used to enhance the localization ability and classification performance. Similarly, the related parameters (kernel sizes, number of neurons, strides, and

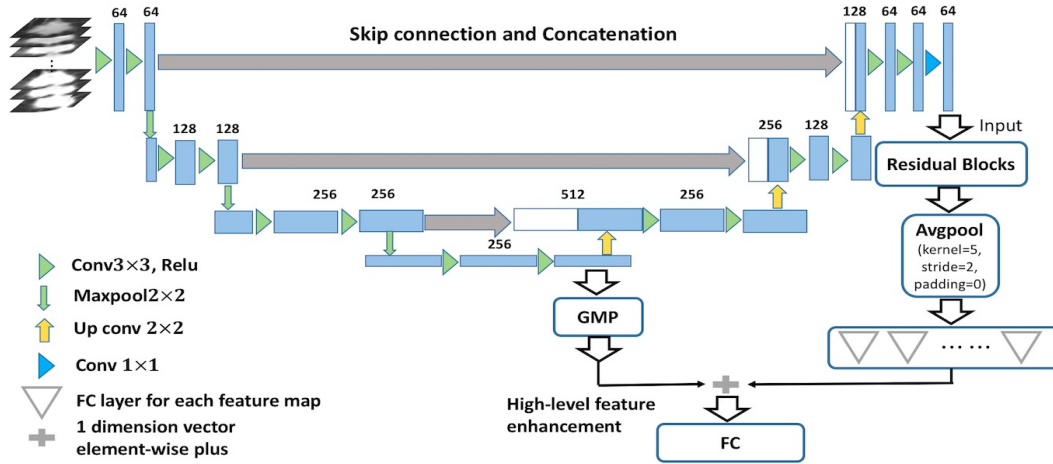


Figure 2: Proposed model with the high-level enhanced SAM. All the Conv layers in the residual blocks followed by BN (Ioffe and Szegedy 2015) and ReLU. GMP and FC represent global maxpooling and fully-connected layers respectively.

padding) of the corresponding layers remain the same. At the output layer of UNet, there is a convolutional (Conv) layer with kernel size 1. Then, the final output is the segmented image of 1 channel. We can specify the number of final  $1 \times 1$  kernels, and feed the resulted 64 feature maps into another residual learning network to extract features (He et al. 2016). Residual blocks in Fig.2 contain two basic blocks with kernel size of 3 for all the Conv layers (He et al. 2016).

Among most of classification tasks accomplished by deep convolutional networks, high-level features fed into classifiers will have a great impact on the final performance since they reflect semantic and discriminative information from CT slices. To utilize these features, we add a Global MaxPooling (GMP) layer after the end of the third down-sampling block which contains 256 feature maps of size  $4 \times 4$ . Hence, the output of the GMP layer is a one dimensional vector consisting of 256 elements. The  $4 \times 4$  high-level feature vector can be decoded to approximate the original image by combining early features through the skip connection (Ronneberger, Fischer, and Brox 2015). Therefore, the 256 dimensional vector can be denoted as an effective representation of the input image in a low dimensional space. Normally, this representation is obtained in the reconstruction task. Then, the parameters are updated based on the reconstruction loss, e.g., Mean Square Error (MSE) and KullbackLeibler (KL) divergency, and the loss value is computed pixel-wise. Hence, an input image can be projected as a code into a lower dimensional subspace, and the code is of high representative value for the input. In our architecture, we use a classification loss, e.g., cross-entropy loss. This is different from the aforementioned reconstruction task, in which our parameters are updated based on class information. In other words, the code learned by the reconstruction loss tends to represent the input itself, and meanwhile the classification loss lets the code to be mostly related to features of the input. Therefore, the final down-sampling code is actually the effective representation of features of the input from a certain class. This feature

related code is used to locate the lesion regions precisely, which will be further discussed below.

Another purpose of our work is to localize lesions where the network pays attention to. As stated in (Zhou et al. 2016), the final Conv features for computing CAMs should be in larger size such as  $13 \times 13$  and  $14 \times 14$ . Thus, the output feature maps of the residual blocks in our model are of size  $16 \times 16$ . Through the AvgPooling layer, each feature map was converted to being of  $6 \times 6$ . After the FC layers with respect to each  $6 \times 6$  feature vector, we obtained a 256 dimensional vector. The sum of this vector and output of GMP provides a satisfactory representation of an input in terms of semantics and spatial structure.

### Soft Activation Mapping (SAM)

CAMs (Zhou et al. 2016) project the final Conv features into single values which highlight the importance of the corresponding features. The obtained activation maps can locate the objects to some extent, which verifies the power of GAP in generating the weights of features. For some nodule lesions at some minor or gracile regions, however, GAP will lose its merit. The proposed soft activation mapping as illustrated in Fig.3 is capable of addressing this problem, and defined as follows:

$$A_k^{x',y'} = a(g_k(x, y)), k \in \{1, 2, \dots, n\}, \quad (3)$$

$$H_k = h_k(A_k), \quad (4)$$

where  $g_k(x, y)$  represents the activation function of unit  $k$  in the last Conv layer (Note that in our model, the last Conv layer in the residual blocks) at a spatial location  $(x, y)$ ,  $g_k$  is the  $k$ th feature map,  $a$  is the average (AVG) pooling layer, and  $A_k^{x',y'}$  represents the result generated by AVG pooling at the spatial location  $(x, y)$  of  $g_k$ . In this study, we call  $A_k$  (features after the final AVG pooling layer) the minor feature, where the value at  $(x', y')$  is mapped from  $(x, y)$ .  $h_k$  denotes the FC layer which follows  $A_k$ , and each  $h_k$  has only one neuron, i.e., every  $H_k$  is a single value. Therefore, the final  $n$  feature maps are projected into  $n$  values. The

input to the softmax, for a given class  $c$ , is  $S'_c$ . The soft activation map  $M'_c$  of class relevance is defined as follows:

$$S'_c = \sum_k \alpha_k^c H_k, \quad (5)$$

$$M'_c = \sum_k \alpha_k^c g_k(x, y). \quad (6)$$

Finally, the output of the softmax for class  $c$  is given by  $\frac{\exp(S'_c)}{\sum_c \exp(S'_c)}$ .  $M'_c$  indicates the importance of activation at a spatial location  $(x, y)$  for classifying an image of class  $c$ .

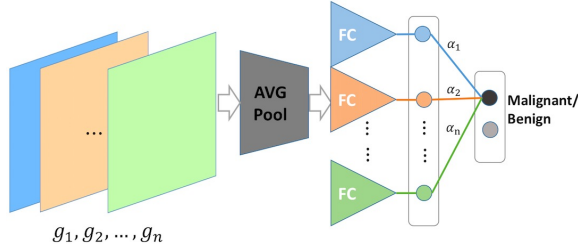


Figure 3: Soft activation mapping (SAM) that reflects class information.

Both CAMs (Zhou et al. 2016) and SAMs assume that the final Conv feature maps contain more valuable and more semantic information on the corresponding input image. Each feature map matches a certain interested part of that class. Then, the linear combination of these features is performed with respect to a group of weights  $(\alpha_k, k \in \{1, 2, \dots, n\})$  in Eq.6, i.e., every one of features contributes differently to the final localization. Nevertheless, the main distinction between these two methods lies in *how to compute the weights related to the corresponding features*. CAM transforms one feature map into one single averaged value over all pixels. This approach avoids low activations that reduce the output of the particular maps and high activations that augment the output of the particular maps, which may happen with global max pooling (GMP). For the specificity of lung nodules, more variations of margin morphology are closely related to categorization of a nodule (Li et al. 2004), and localization of various changing patterns cannot be easily resolved by CAMs that capture the extent of regions, since GMP misses the variations in wider ranges.

In our SAM, we do not directly project feature maps into their respective single value. By average pooling, some high activations that reflect discriminative features can be averaged just in small receptive fields of pooling operation. Minor features (feature maps after AVG pooling) maintain in regions of high/low activations. The subsequent FC layers project the minor features into single values, i.e., the weights for generating class activation maps. These weights can be projected back onto the final Conv features. That is to say, weights in SAM are optimized in the learning process. In fact, if the final Conv features are fed into standard FC layers together, the large amount of parameters will result in overfitting. However, the number of parameters of SAM is reduced by adding FC layers to each feature map.

**High-level enhanced SAMs (HESAMs).** Feature maps from the final Conv layers of the residual blocks are in larger size, since they cover most of the lesion regions (shape variations). SAM maintains semantic features according to high/low activations. However, some regions corresponding to middle activations of two categories will mislead the classifier, which can be seen in Fig.6. In order to avoid this problem and improve the performance of our model, we add high-level enhanced representations to the weights generated by SAM (HESAM). The input to the softmax and soft activation maps are refined as follows:

$$S'_c = \sum_k (\alpha_k^c + d_k^c) H_k, \quad (7)$$

$$M'_c = \sum_k (\alpha_k^c + d_k^c) g_k(x, y), \quad (8)$$

where  $d_k, k \in \{1, 2, \dots, n\}$  are representations of high-level features generated by GMP (Fig.2). We will aggregate the information most relevant to categorization specificity with the SAMs, and not let  $d_k$  impact fully on the weights. In other words, Eq.7 performs  $\sum_k d_k^c H_k$  on prior  $S'_c$  and Eq. 8 performs  $\sum_k d_k^c g_k(x, y)$  on prior  $M'_c$ . In fact, these two items act as auxiliary enhancements for class specific representations. The sequence of  $d_k$  needs not to be matched to that of  $\alpha_k$ .

## Experiments

In this section, we evaluate the performance of our model, SAM and HESAM on LIDC-IDRI (Armato III et al. 2011) dataset. Experiments show that our proposed models achieve higher classification accuracy and more accurate lesion region localization compared with several state-of-the-art models. All of our experiments are implemented on 2 NVIDIA GTX 1080 Ti GPUs.

### Data Preparation

LIDC-IDRI is a publicly available dataset of pulmonary nodules from 1010 patients who underwent chest CT LIDC. Each nodule was rated from 1 to 5 by four experienced thoracic radiologists, indicating an increasing probability of malignancy. In this study, the ROI of each nodule was obtained along with its annotated center in accordance with the nodule report, with a square shape of a doubled equivalent diameter. An average score of a nodule was used for assigning probability of malignant etiology. Nodules with an average score higher than 3 were labeled as malignant and lower than 3 are labeled as benign. Some nodules were removed from the experiments in the case of the averaged malignancy score 3, ambiguous IDs, and being rated by only one or two radiologist. All images were resampled to have  $1mm$  spacing (original spacing ranged from  $0.6mm$  to  $3.0mm$ ) in the z-dimension with  $512 \times 512$  matrices. Finally, the dataset consists of 635 benign and 510 malignant nodules. All experiments are conducted through 5-fold cross validation.

In addition, our model requires the input with *channel*  $\in \{1, 3, 11, 21\}$ . Therefore, we construct 4 datasets (Tab.2) to evaluate how the performance of deep networks can be

Table 1: Classification accuracies (%) on four benchmark datasets. Values of sensitivity and specificity are obtained based on D\_11C dataset.  $\bullet$ -CAM and  $\bullet$ -SAM denote that corresponding networks performed the following modifications to generate larger feature maps ( $16 \times 16$ ) at the last Conv layer. ResNet-CAM/SAM: reduce the last pooling layer and strides in each residual block are set as 1; VGG16-CAM/SAM: delete the last 4 pooling layers and number of FC layers is reduced to 1; DenseNet-CAM/SAM: delete the final pooling layer and strides of pooling in transition block are reduced to 1.

Method	D_1C	D_3C	D_11C	D_21C	Sensitivity	Specificity
PN_SAMP (Wu et al. 2018)	84.28	91.70	97.82	97.38	0.8431	0.9763
ResNet18 (He et al. 2016)	81.22	91.27	95.63	95.79	0.9411	0.9685
ResNet34 (He et al. 2016)	80.79	90.83	96.07	95.20	0.9705	0.9763
VGG16 (Simonyan and Zisserman 2015)	<b>85.59</b>	91.70	96.69	96.07	0.9411	0.9763
DenseNet121 (Huang et al. 2017)	79.91	87.77	93.45	90.83	0.9215	0.9527
ResNet18-CAM	81.66	88.21	95.36	95.20	0.9216	0.9764
ResNet34-CAM	81.66	86.90	97.82	96.94	0.9509	0.9781
VGG16-CAM	83.41	89.96	92.14	91.70	0.9117	0.9448
DenseNet121-CAM	80.35	86.46	95.63	89.08	0.9313	0.9527
ResNet18-SAM	84.28	89.96	97.38	96.94	0.9607	0.9763
ResNet34-SAM	83.41	88.69	98.25	96.51	0.9509	0.9843
VGG16-SAM	83.41	90.83	94.32	93.89	0.9411	0.9448
DenseNet121-SAM	81.22	88.65	97.28	94.76	0.9411	0.9685
Ours-CAM	80.35	86.46	96.51	95.20	0.9509	0.9737
Ours-SAM	81.66	89.08	98.25	97.38	0.9509	0.9843
Ours-HESAM	83.41	<b>92.58</b>	<b>99.13</b>	<b>98.69</b>	<b>0.9705</b>	<b>0.9921</b>

impacted by different input channels of nodule volume. As illustrated in Tab.2, image resolution of all patches is  $32 \times 32$ . The D\_3C dataset comprises patches with the square shape of  $p \times diameter$ ,  $p \in \{2, 3, 4\}$  around the annotated center, and each input sample consists of 3 patches corresponding to 3 channels.

Table 2: Settings of constructed datasets with different channels:  $\{numofimage, channel, height, width\}$

Dataset	Train	Test
D_1C	{916, 1, 32, 32}	{229, 1, 32, 32}
D_3C	{916, 3, 32, 32}	{229, 3, 32, 32}
D_11C	{916, 11, 32, 32}	{229, 11, 32, 32}
D_21C	{916, 21, 32, 32}	{229, 21, 32, 32}

### Nodule Classification Using Volume Data

In this section, we firstly conduct classification experiments using 4 mentioned datasets, and the input channel for all models varies from related dataset. For all methods, the other parameters are set as follows: learning rate is 0.0005, batch size is 32, and weight decay is 0.0001. The loss function is cross-entropy loss and optimizer is stochastic gradient decent (SGD).

**Classification performance.** All the models in our experiments are trained using 4 datasets. As illustrated in Tab.1, for all methods, accuracies of using D\_11C and D\_21C are higher than those of using D\_1C and D\_3C, and our method achieves higher specificity (from 0.5% to 5%) than others. This demonstrated that various features in multiple slices enhanced the representation of a nodule volume. Actually, increase of channels reflects that abundant information of lesion regions are learned at the same time, i.e., at first

convolution layer, each filter convolves an input at transverse plane across all channels. Then, the final convolutional result is the aggregation of results with respect to all channels. In the case of D\_1C, features extracted by the first convolution layer have less structural diversity than those of other 3 datasets. D\_3C fuses the multi-scale information into feature learning even maps of 3 channels of an input are based on one slice, but the edge variations of nodule in other slices are ignored. D\_11C and D\_21C ensemble both shape variations and multi-scale information and the classification results outperform the other two datasets. We can observe that accuracies on D\_21C are a slightly lower than those of D\_11C for all methods, and this is probably because more channels of slices which are far from center slice contain more similar background information. Consequently, features for samples of both categories possess some common parts, impairing the performance of classifier.

**Alleviating overfitting through multi-slices input.** We use multi-slices data to instead manual data augmentations which are tailored for reducing overfitting. From testing results (Fig. 4) we can see that all the methods will not converge better when using D\_1C dataset. This phenomenon can also be observed in D\_3C, although overfitting is slightly reduced. Note that in D\_11C and D\_21C, overfitting has a large decrease, and test loss decreases except DenseNet 121. Although overfitting of VGG16 happens in all datasets, the test loss is decreased in fact and the corresponding test accuracies improve significantly with the increase of input channels.

DenseNet121 is the deepest structure in our experiments. Theoretically, it should learn more useful and accurate features. This is experimentally justified based on D\_1C dataset, and the test loss of DenseNet121 is the second

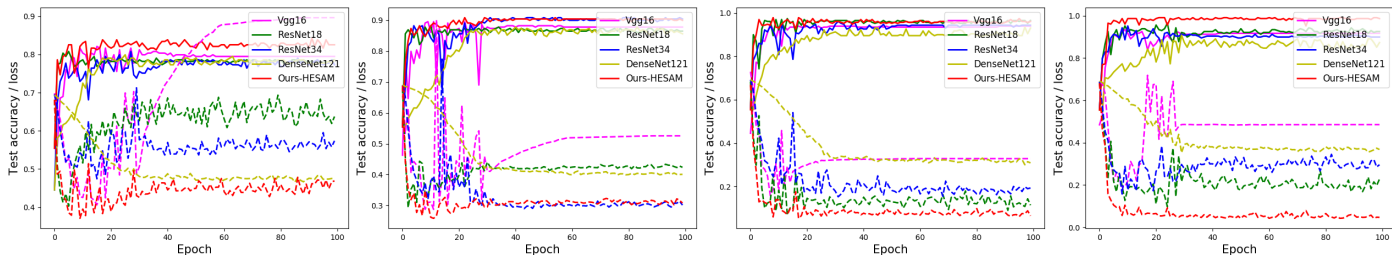


Figure 4: Test performance on 4 constructed datasets. From left to right: D\_1C, D\_3C, D\_11C, D\_21C. Solid lines and dashed lines denote the test accuracies and test losses, respectively.

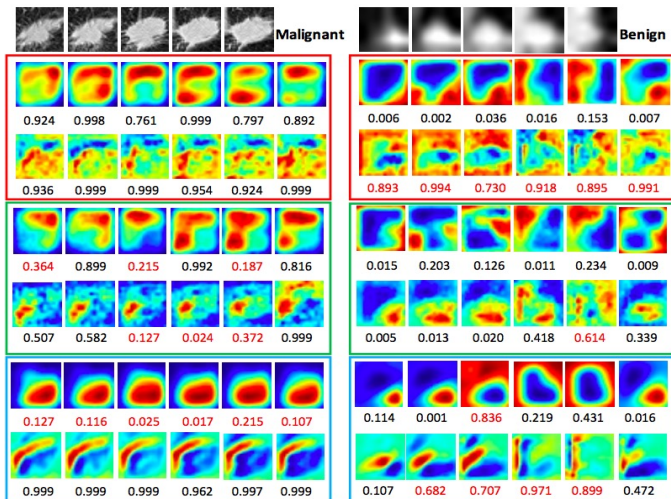


Figure 5: CAMs and SAMs obtained by models that are trained on D\_11C. Each nodule is illustrated 5 of 11 slices. CAMs and SAMs at corresponding positions are obtained by feeding the volume of 11 channels (duplicated single slice) into according models. Final column of each color block is the result obtained by feeding volume of all 11 adjacent slices. Red, green and blue block denotes the results generated by ResNet18-CAM/SAM, ResNet34-CAM/SAM and VGG16-CAM/SAM, respectively. First row of each block shows CAMs and second row shows SAMs. Values are predictions of malignant category. Red color numerics represent false positive (FP) benign nodules and false negative (FN) malignant nodules.

lowest among all methods. The increase of input channels makes few contributions to improve the performance of DenseNet121, which relates to the reason that deeper networks require more training data. Although the first convolution layer is able to extract diverse and robust representation via multiple slices, this advantage will be weakened with the increase of depth of model.

### Comparison Between CAM and SAM

CAM is difficult to localize fine-grained objects. SAM solves this problem effectively by projecting final feature maps into corresponding weights in a soft manner. The weights are updated separately and SAM maintains speci-

ficity of each feature. We applied ResNet18-CAM/SAM, ResNet34-CAM/SAM and VGG16-CAM/SAM (Tab.1) to demonstrate distinction between CAM and SAM. Most of the methods in Tab.1 achieve better performance when using SAM, and this can further justify that SAM indeed pays more attention to distinctive lesion regions than CAM. In addition, fine-grained regions are preserved which can be seen in Fig.5.

As illustrated in Fig.5, CAMs localize on malignant and benign nodules at a larger area, i.e., coarse regions of lesion. SAMs can localize on relatively fine-grained lesion regions which are exhibited apparently discontinuous localizations of margins and micro-regions. However, SAMs also result in false negatives (FNs) and false positives (FPs), which will be avoided by HESAM. CAMs and SAMs of each single slice are different from each other. This demonstrates that the models pay attention to different regions of each slice. The results of a whole volume cover attention regions of all single slices. That is why the performances of each model increase along with growing input channels (Tab.1). Discriminative information in all slices makes great contributions to the performance improvement. Each model learnt different features for both categories of nodules and focused on varying regions. Most distinguishing feature was variations in margin of malignant nodules, whereas most benign nodules demonstrate smoother contour compared to malignant nodules.

### CAM, SAM and HESAM on Our Model

This experiment verifies the effectiveness of high-level feature enhancing operation.

Maps in same positions in Fig.6 have same meaning with those in Fig.5. The CAM and SAM versions of our model (Ours-CAM, Ours-SAM) have turned into using only final residual learning features or minor features to make classification. As shown in Fig.6, CAMs localize not only on some of edges but also on part of nodule bodies. Consequently, this results in high FNs and FPs. SAMs performed as imagined to focus on edges and variations of shapes, which is benefited from separately updated parameters and from local information/structure preserved by average pooling without GAP. Note that unlike CAM, FNs and FPs of SAM mainly locate at margins of nodules rather than their bodies. The phenomenon above is caused by final residual learning features which are unable to learn more discriminative infor-

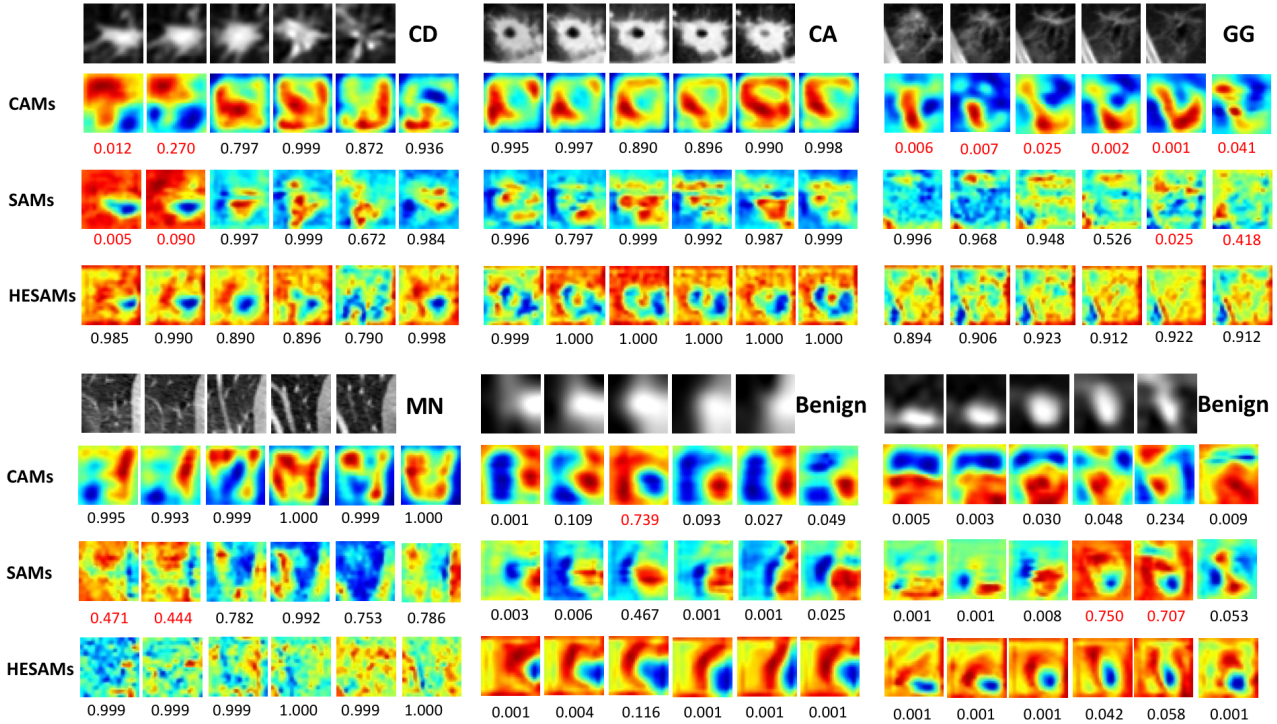


Figure 6: CAMs, SAMs and HESAMs of CD, CA, GG, MN and two benign nodules, which are generated by 3 versions of our model trained on D\_11C. Values under each map are predictions of malignant category. Red color numerics represent false positive (FP) benign nodules and false negative (FN) malignant nodules negatives.

mation with respect to some special cases (such as shape variations and edges blurring). In other word, CAM and SAM lose some class specific information which is critical for lesion localization.

HESAM reapplies the high-level class specific features for localization and improves the classification accuracies simultaneously (Tab.1). HESAM rectifies or augments the results of SAM which are illustrated in the third and the forth rows of each nodule in Fig.6. HESAM and SAM have the same advantage that they can localize on discontinuous and more correct lesion regions of malignant nodules, and focus on regions of smooth and larger area of benign nodules. The shortage of SAM is that it is not able to cover all lesions just as HESAM does. The advantage of localizing on fine-grained morphology variations of HESAM is apparently displayed in CD, CA, MN and GG (Fig.6). The irregular spiculation and cavity are localized completely. For GG and MN, CAM and SAM prefer to search the area where the variations are relatively smooth.

From Tab.1, we can see that HESAM method exhibits outstanding and robust performance on all datasets. Note that overfitting cannot be avoided on D\_1C as well. With the increase of input channels, our model achieves significant improvement and the results are similar on D\_11C and D\_21C. Through the advantage of utilizing classification loss for our model, the code of down-sampling layer is updated between early and final up-sampling features,

i.e., this code focuses more on distinctions between two classes and gets rid of the interference factor of common backgrounds. Hence, the better performance of model is obtained.

All the experiments in Fig.5 and Fig.6 illustrate that volumes consists of same single slices are more likely to be misclassified and mislocalized when using CAM and SAM. HESAM performs better even on volumes of single slices. The class predictions of these volumes are more accurate than those of CAM and SAM.

## Conclusion

Our paper proposes a novel method for fine-grained lung lesion localization through soft activation mapping (SAM). Our method has accurate localization and better classification of nodules coupled with high-level features from the classification loss of the UNet model. Testing on the LIDC-IDRI dataset suggests that feeding multiple-slices into 2D networks can alleviate the overfitting problem. Our model has outperformed representative state-of-the-art models in terms of false positive rate. However, our model depends on the extraction of high-level features from an auto-encoder based architecture, and dimensions of high-level features and final weights must be the same. In future, we will apply more adaptive methods for further improvement of the lung LDCT screening and diagnostic performance.

## References

- Ahonen, T.; Hadid, A.; and Pietikainen, M. 2007. Face description with local binary patterns: Application to face recognition. *IEEE Transactions on Pattern Analysis and Machine Intelligence (TPAMI)* 28(12):2037–2041.
- Armato III, S. G.; McLennan, G.; Bidaut, L.; et al. 2011. The lung image database consortium (LIDC) and image database resource initiative (IDRI): A completed reference database of lung nodules on CT scans. *Medical Physics* 38(2):915–931.
- Çiçek, Ö.; Abdulkadir, A.; Lienkamp, S. S.; Brox, T.; and Ronneberger, O. 2016. 3D U-Net: learning dense volumetric segmentation from sparse annotation. In *International Conference on Medical Image Computing and Computer-Assisted Intervention (MICCAI)*, 424–432.
- Dou, Q.; Chen, H.; Yu, L.; Qin, J.; and Heng, P.-A. 2017. Multilevel contextual 3D CNNs for false positive reduction in pulmonary nodule detection. *IEEE Transactions on Biomedical Engineering (TBE)* 64(7):1558–1567.
- Hara, K.; Kataoka, H.; and Satoh, Y. 2018. Can spatiotemporal 3D CNNs retrace the history of 2D CNNs and Imagenet. In *Proceedings of the IEEE Conference on Computer Vision and Pattern Recognition (CVPR)*, 18–22.
- He, K.; Zhang, X.; Ren, S.; and Sun, J. 2016. Deep residual learning for image recognition. In *The IEEE Conference on Computer Vision and Pattern Recognition (CVPR)*.
- Huang, G.; Liu, Z.; v. d. Maaten, L.; and Weinberger, K. Q. 2017. Densely connected convolutional networks. In *2017 IEEE Conference on Computer Vision and Pattern Recognition (CVPR)*, 2261–2269.
- Hussein, S.; Gillies, R.; Cao, K.; Song, Q.; and Bagci, U. 2017. Tumornet: Lung nodule characterization using multi-view convolutional neural network with Gaussian process. In *2017 IEEE 14th International Symposium on Biomedical Imaging (ISBI)*, 1007–1010.
- Ioffe, S., and Szegedy, C. 2015. Batch normalization: Accelerating deep network training by reducing internal covariate shift. In *Proceedings of the 32nd International Conference on International Conference on Machine Learning (ICML)*, volume 37, 448–456.
- Lei, Y.; Zhao, X.; Wang, G.; Yu, K.; and Guo, W. 2017. A novel approach for cirrhosis recognition via improved LBP algorithm and dictionary learning. *Biomedical Signal Processing and Control* 38:281 – 292.
- Li, F.; Sone, S.; Abe, H.; MacMahon, H.; and Doi, K. 2004. Malignant versus benign nodules at CT screening for lung cancer: comparison of thin-section CT findings. *Radiology* 233(3):793–798.
- Lin, M.; Chen, Q.; and Yan, S. 2014. Network in network. In *International Conference on Learning Representations (ICLR)*.
- Ritter, S.; Barrett, D. G.; Santoro, A.; and Botvinick, M. M. 2017. Cognitive psychology for deep neural networks: A shape bias case study. In *Proceedings of the 34th International Conference on Machine Learning (ICML)*.
- Ronneberger, O.; Fischer, P.; and Brox, T. 2015. U-net: Convolutional networks for biomedical image segmentation. In *International Conference on Medical Image Computing and Computer-Assisted Intervention*, 234–241.
- Setio, A. A. A.; Ciompi, F.; Litjens, G.; et al. 2016. Pulmonary nodule detection in CT images: false positive reduction using multi-view convolutional networks. *IEEE Transactions on Medical Imaging (TMI)* 35(5):1160–1169.
- Shan, H.; Wang, G.; Kalra, M. K.; de Souza, R.; and Zhang, J. 2017. Enhancing transferability of features from pretrained deep neural networks for lung nodule classification. In *The Proceedings of the 2017 International Conference on Fully Three-Dimensional Image Reconstruction in Radiology and Nuclear Medicine (Fully3D)*, 65–68.
- Shan, H.; Zhang, Y.; Yang, Q.; Kruger, U.; Kalra, M.; Sun, L.; Cong, W.; and Wang, G. 2018. 3-d convolutional encoder-decoder network for low-dose ct via transfer learning from a 2-d trained network. *IEEE Transactions on Medical Imaging (TMI)* 37(6):1522.
- Shen, W.; Zhou, M.; Yang, F.; Yang, C.; and Tian, J. 2015. Multi-scale convolutional neural networks for lung nodule classification. In *International Conference on Information Processing in Medical Imaging (IPMI)*, 588–599.
- Shin, H.; Roth, H. R.; Gao, M.; Lu, L.; Xu, Z.; Nogues, I.; Yao, J.; Mollura, D.; and Summers, R. M. 2016. Deep convolutional neural networks for computer-aided detection: CNN architectures, dataset characteristics and transfer learning. *IEEE Transactions on Medical Imaging (TMI)* 35(5):1285–1298.
- Simonyan, K., and Zisserman, A. 2015. Very deep convolutional networks for large-scale image recognition. In *International Conference on Learning Representations (ICLR)*, 1–14.
- Team, N. L. S. T. R. 2011. Reduced lung-cancer mortality with low-dose computed tomographic screening. *New England Journal of Medicine* 365(5):395–409.
- WHO. 2011. Description of the global burden of NCDs, their risk factors and determinants. *Global Status Report on Noncommunicable Diseases 2010*, 1–176.
- Wu, B.; Zhou, Z.; Wang, J.; and Wang, Y. 2018. Joint learning for pulmonary nodule segmentation, attributes and malignancy prediction. In *2018 IEEE 15th International Symposium on Biomedical Imaging (ISBI)*, 1109–1113.
- Zhou, B.; Khosla, A.; Lapedriza, A.; Oliva, A.; and Torralba, A. 2016. Learning deep features for discriminative localization. In *2016 IEEE Conference on Computer Vision and Pattern Recognition (CVPR)*, 2921–2929.